Report
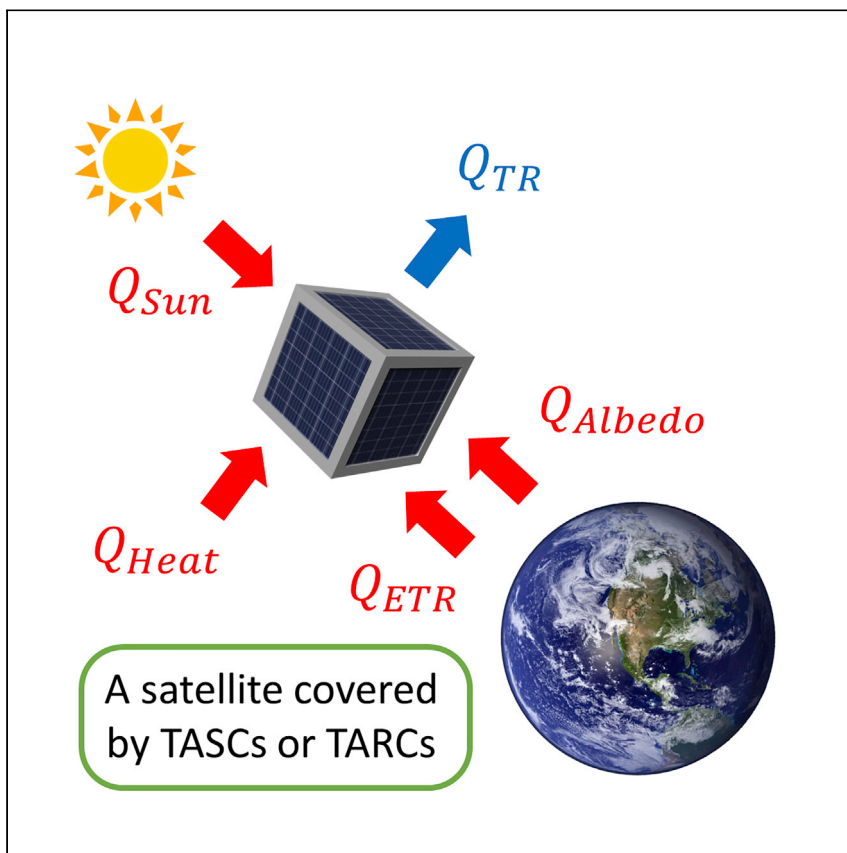
Reducing temperature swing of space objects with temperature-adaptive solar or radiative coating

A satellite covered by TASCs or TARCs

Advanced high-performance passive temperature management technologies without additional mass/volume/power burdens are required for space exploration. Dong et al. propose use of emerging temperature-adaptive solar or radiative coatings (TASCs or TARCs, respectively) on space objects and simulate their temperature-regulation performance with satellite thermal models, demonstrating the potential of TARCs and TARCs in outer space.

Kaichen Dong, Derick Tseng, Jiachen Li, Sorren Warkander, Jie Yao, Junqiao Wu

wuj@berkeley.edu

Highlights

TASCs and TARCs are promising for passive temperature management in outer space

TASCs and TARCs do not bring in extra mass, volume, or power burdens to spacecrafts

The thermal performance of TASCs and TARCs is simulated with satellite thermal models

Simulations show a temperature swing as low as 5.3°C in a 1U-CubeSat covered by TARCs

CellPress
OPEN ACCESS

Report

Reducing temperature swing of space objects with temperature-adaptive solar or radiative coating

Kaichen Dong,[1,2] Derick Tseng,[1] Jiachen Li,[1,2] Sorren Warkander,[1,2] Jie Yao,[1,2] and Junqiao Wu[1,2,3,*]

SUMMARY

Lacking the atmosphere for temperature neutralization, objects in outer space without thermal control undergo large temperature swings. Effective temperature management technologies (TMTs) are essential to avoid undesirable effects caused by extreme thermal conditions. However, existing high-performance TMTs impose additional burden on the limited mass and power budgets of spacecrafts. Very recently, temperature-adaptive solar coatings (TASCs) and temperature-adaptive radiative coatings (TARCs) emerged as novel light-weight, energy-free temperature-regulation approaches for terrestrial objects with excellent thermal performance. Here, we simulate and present the great potential of TASCs and TARCs as future passive TMTs for space objects. A case study of a geosynchronous satellite with body-mounted solar panels covered by TARC exhibits an interior temperature swing as small as 20.3°C–25.6°C in an orbital period even with solar eclipses. These findings provide insight into the superior performance of TASCs and TARCs in space and will promote their application in extraterrestrial missions.

INTRODUCTION

Temperature maintenance and regulation are vital to spacecrafts and astronauts due to the extremely hostile environments in space.[1,2] The temperature of a space object can easily change by many hundreds of degrees ($-220°C$ to $+220°C$) depending primarily on solar irradiance received by and heat radiated from the object,[2] imposing fatal threats to all components and crew (for manned space missions).[3,4] Moreover, such high temperature swings also introduce instrumental misalignment,[5] large noise signals,[6,7] and thermal cycling damages to mechanical structures.[8] To ensure normal operation of components and survival of crew, massive temperature swings must be avoided by advanced thermal management technologies (TMTs).[9,10]

Existing TMTs that have already been applied to space objects (including spacecrafts and spacesuits) are categorized as active and passive strategies according to their need for power input. Active TMTs—including electrical heaters,[11] cryocoolers,[12] thermoelectric coolers,[13] and fluid loops[14]—consume electricity to provide accurate temperature control of space objects. However, they typically require extra mass, volume, and power, so they are generally only used with high heat loads in large spacecrafts.[10] On the contrary, passive TMTs offer power-free control of temperatures and are thus favorable in power-sensitive and small space objects. However, conventional passive TMTs—such as paints and coatings,[15] multi-layer insulation materials,[16] and sun shields[17]—are limited by their static radiative heat transfer properties and are thus incapable of reducing both the high and low

[1]Department of Materials Science and Engineering, University of California, Berkeley, Berkeley, CA 94720, USA

[2]Materials Sciences Division, Lawrence Berkeley National Laboratory, Berkeley, CA 94720, USA

[3]Lead contact

*Correspondence: wuj@berkeley.edu

https://doi.org/10.1016/j.xcrp.2022.101066

temperature extremes in thermal cycles. Some advanced passive TMTs—like passive thermal louvers,[18] deployable radiators,[19] thermal switches,[20] and phase-change thermal storage units[21]—have been employed for temperature-adaptive thermal control, but unfortunately, they come at the cost of high extra mass and volume. It is therefore essential to develop a high-performance passive TMT without additional mass and volume requirements.

Very recently, temperature-adaptive radiative coatings (TARCs) were invented,[22–28] which "intelligently" and automatically adjust their thermal radiation according to surface temperatures. At high temperatures, they strongly emit thermal radiation to dissipate heat into outer space; at lower temperatures, they automatically turn off radiation to retain heat. The solar absorptivity of TARCs is temperature independent. Neither power input nor manual intervention are required during this process. Though first invented for terrestrial objects like house roofs, this emerging technology shows great potential in space applications. Such thin, flexible, light-weight, and power-free coatings are expected to dramatically reduce the temperature swings experienced by space objects.[22,25,26]

In this work, we systematically simulated the temperature-regulation performance of temperature-adaptive coatings in space missions with three different models: (1) a two-dimensional (2D) flat surface, (2) a 3D cube (regular hexahedron), and (3) a geosynchronous 1U-CubeSat[29] orbiting Earth. In those models, temperature-adaptive solar coatings (TASCs) and TARCs were compared. TASCs work in a similar way as TARCs except that their solar absorptivity, as opposed to thermal emissivity, is switched in response to temperature change, while their thermal emissivity stays a constant. Both TASCs and TARCs significantly cut down the temperature swing compared with the original surface of the space object that is not temperature adaptive. Because the only thermal interaction with the environment in space is electromagnetic radiation, we found that although the relative advantages between TASCs and TARCs vary from mission to mission, TARCs evidently outperform TASCs for Earth satellites in orbits with solar eclipses. Furthermore, we simulated the scenarios where TASCs and TARCs hypothetically have 100% transmission in the wavelength range of 0.4–1.1 μm so that they can cover the solar panels (SPs) of spacecrafts without influencing the SP performance.[30,31] We revealed that the performance in limiting the temperature swing deteriorates for TASCs but remains nearly the same for TARCs. The above analyses were followed by a case study where a geosynchronous CubeSat is covered by an experimentally demonstrated TARC (hereafter called a "real-TARC") with published data.[22] In-depth, transient thermal analysis of body-mounted SPs and interior satellite components were conducted, showing the extraordinary performance of TARCs in reducing temperature swings. As such, TARCs show great promise as a new passive TMT in space missions and offer new temperature-regulation solutions for a diverse range of space objects such as space stations, satellites, spacesuits, and even extraterrestrial bases.[32]

RESULTS AND DISCUSSION

Temperature swings of space objects

The extraterrestrial (AM0) solar spectrum[33] and a typical black-body radiation spectrum are shown in Figure 1A. Unlike the terrestrial thermal emitters that are limited in and optimized for the 8–13 μm atmospheric transparency window,[34] the thermal emitters in space are not spectrally limited due to the vacuum environment. As a result, the energy flux of thermal radiation is enhanced for objects in space to a level

CellPress
OPEN ACCESS
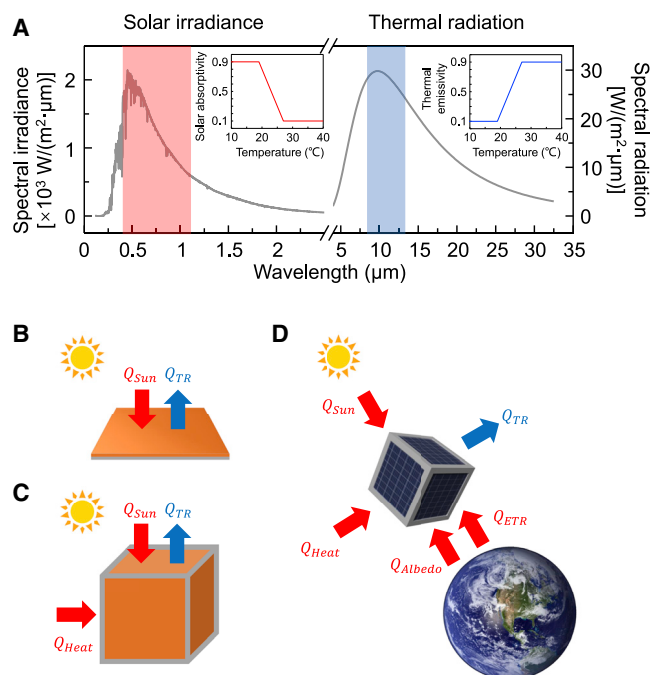
Figure 1. Theoretical schemes

(A) Spectra of AM0 solar irradiance (left) and black-body radiation at 23°C calculated by Planck's law (right). The red and blue boxes indicate the ideal 100% transmission band for TASCs or TARCs covering solar panels and the atmospheric transmission window for terrestrial thermal emitters, respectively. Inset: temperature-adaptive solar absorptivity of TASCs (left) and temperature-adaptive thermal emissivity of TARCs (right) analyzed in this work.
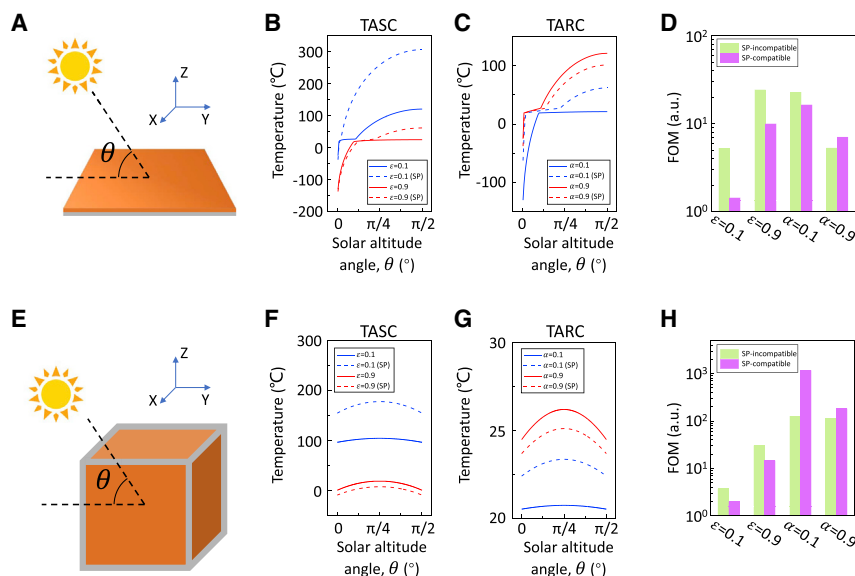
(B–D) Schematic diagrams of the 2D board model (B), the 3D cube model (C), and the CubeSat model (D). Q_{Sun}, Q_{TR}, Q_{Heat}, Q_{Albedo}, and Q_{ETR} are heat transfer power from solar irradiance (heating), thermal radiation of the CubeSat (cooling), interior satellite components (heating), Earth albedo (heating), and thermal radiation of Earth (heating), respectively.

that could outweigh the solar heating, which necessitates the comparison between TASCs and TARCs in their temperature-regulation performance in outer space.

Hence, we compared temperature swings of space objects using eight different TASCs and TARCs whose solar absorptivity (α) and thermal emissivity (ε) are defined as follows (see Table S3 for details):

(1) TASCs with a switchable α and a low ε (0.1) or a high ε (0.9).
(2) SP-compatible TASCs with a switchable α and a low ε (0.1) or a high ε (0.9).
(3) TARCs with a switchable ε and a low α (0.1) or a high α (0.9).
(4) SP-compatible TARCs with a switchable ε and a low α (0.1) or a high α (0.9).

The switchable α of TASCs and switchable ε of TARCs are shown in the left and right insets of Figure 1A, respectively. The 19°C–27°C temperature range for the switching transition is taken from previous work,[22] and the target temperature for stabilization is T_{set} = 23°C in the middle of the switching range (Note S1; Table S1). Since spacecrafts, especially miniature satellites, are power-efficient systems equipped with large-area body-mounted SPs,[35] the compatibility with SPs will significantly expand the total applicable area of TASCs or TARCs on spacecrafts. In our simulation, SP-compatible TASCs and TARCs are those that have everything else the same as the normal TASCs and TARCs but with 100% transmittance over the primary spectral response range (0.4–1.1 μm) of photovoltaics (PVs)[30,31] so that they can be applied on top of SPs

Figure 2. Fundamental thermal analysis models for TASCs and TARCs

(A) A schematic diagram of the 2D board model.

(B and C) Static surface temperatures as functions of θ for boards covered by TASCs (B) or TARCs (C), where SP represents SP compatible.

(D) Extracted FOMs for the cases in (B) and (C).

(E) A schematic diagram of the 3D cube model.

(F and G) Static surface temperatures as functions of θ for cubes covered by TASCs (F) or TARCs (G), where SP represents SP compatible.

(H) Extracted FOMs for the cases in (F) and (G).

(Note S2; Figure S1). Note that in this simulation, the SPs beneath SP-compatible TASCs or TARCs are assigned with a PV efficiency of 25% and a reflectance of 10%,[36,37] leading to 65% of the solar energy in 0.4–1.1 μm converted into heat in SPs for SP-compatible cases. Apart from that 0.4–1.1 μm range in the SP-compatible scenario, all TASCs and TARCs have 0% transmittance in both solar and thermal spectra. The above coatings were analyzed using three different models (Figures 1B–1D).

We first calculated the surface temperature of a 2D board in space under solar irradiance (Figure 1B), with the top surface covered by TASC or TARC and the bottom surface completely insulated from the environment. Such a 2D board can be considered as a basic component of various 3D objects, thus providing valuable information on the behavior of more complex objects. A thermal equilibrium state is achieved when the Q_{Sun} equals Q_{TR} at the top surface:

$$\begin{cases} Q_{Sun}(\theta, T) = Q_{TR}(T) \\ Q_{Sun}(\theta, T) = H_{Sun} \times \sin \theta \times \alpha(T) \times A \\ Q_{TR}(T) = \left(H_{SB}(T) - H_{SB}(T_{space})\right) \times \varepsilon(T) \times A \end{cases}, \qquad \text{(Equation 1)}$$

where H_{Sun} = 1,367 W/m² is the solar energy heat flux for Earth satellites[38] and $H_{SB}(T)$ is the black-body radiation flux by the Stefan-Boltzmann's law.[38–40] With a background space temperature of T_{space} = 2.7 K,[39,40] the static surface temperature T as a function of solar altitude angle θ (Figure 2A) is calculated for all TASCs and TARCs, and the results are compared in Figures 2B and 2C (see Note S3 and Figures S2 and S3 for more details). Note that all temperatures at $\theta = 0°$ are 2.7 K and thus are excluded from the plots for clarity. Most spacecraft components achieve optimal performance near room temperatures (Note S1), so we define the dimensionless figure of merit (FOM) for temperature management as

Cell Reports
Physical Science
Report

CellPress
OPEN ACCESS

$$FOM = \frac{T_{set} \times \int_0^{\pi/2} d\theta}{\int_0^{\pi/2} |T(\theta) - T_{set}| d\theta}. \qquad \text{(Equation 2)}$$

Obviously, the FOM describes the relative extent of T deviating from T_{set} integrated over an entire period. A high value of FOM is desired, as it indicates a small temperature swing in the space mission. The FOM would be equal to infinity if the temperature swing is ideally zero (T is constant and $= T_{set}$), close to 1 if the temperature is constant and near 0 K, and approaching zero if the temperature experiences a very large swing ($|T(\theta) - T_{set}| \gg 0$).

Due to the broadband thermal emission in space, the temperature swings for the cases of TASCs and TARCs are similar in Figures 2B and 2C. This differs substantially from terrestrial scenarios where solar heating power dominates over thermal radiation because the latter is limited to a narrow sky window.[34] Another conclusion is the static ε (α) should be optimized to achieve smaller temperature swings for TASCs (TARCs): one order-of-magnitude change in FOM can be found between optimized and unoptimized TASCs and TARCs (Figure S3). Moreover, when temperature-adaptive coatings are made SP compatible to cover SPs, the temperature-management performance of TASCs worsens due to the non-temperature-adaptive α in the 0.4–1.1 μm band. The FOM of TASC ($\varepsilon = 0.1$ or 0.9) is decreased by a factor of 3.7 or 2.4 when SP compatibility is enforced.

To better identify the temperature swing of actual 3D objects, we then simulated a cube whose six surfaces are all covered by identical TASCs or TARCs (Figure 1C). The static temperature for such a cube is calculated by

$$\begin{cases} Q_{Sun}(\theta, T) + Q_{Heat} = Q_{TR}(T) \\ Q_{Sun}(\theta, T) = H_{Sun} \times (\sin\theta + \cos\theta) \times \alpha(T) \times A \\ Q_{TR}(T) = (H_{SB}(T) - H_{SB}(T_{space})) \times \varepsilon(T) \times A \times 6 \end{cases} \qquad \text{(Equation 3)}$$

Based on the typical design of a 1U-CubeSat, the area of each surface (A) is set at 0.01 m²[.29] Here, the CubeSat is assumed to be in the "working" mode with high power consumption throughout the simulated period, and the interior heating power (Q_{Heat}) is set at a constant 5 W.[41,42] In our calculation, for simplicity, the sunbeam direction is in the yz plane (Figure 2E), i.e., it is normal to the −y and +z cube surfaces when $\theta = 0°$ and $\pi/2$, respectively.

Though Figures 2F and 2G verify that both TASCs and TARCs help reduce the temperature swings, TARCs excel in maintaining a smaller temperature swing because the total physical area of thermal emission (all six surfaces) greatly exceeds that of solar absorption (three surfaces at most), regardless of SP compatibility (Figure 2H). The FOM of SP-compatible TASC ($\varepsilon = 0.1$) is surprisingly 99.8% lower than that of the SP-compatible TARC ($\alpha = 0.1$). Calculation details and results with other sunbeam directions can be found in Note S4 and Figures S4 and S5.

Additionally, we conducted a more comprehensive thermal analysis by calculating the transient temperature of a geostationary 1U-CubeSat when the Earth is at the December solstice (Figure 3A). In such an orbit, the CubeSat does not experience solar eclipses. Note that in this model we do not consider the inhomogeneous temperature distribution inside the CubeSat. The orbital period of the CubeSat is ~1,436 min, and the revolution of the Earth is not considered. The calculation starts at $t = −24$ h, and the CubeSat is at position p_0 with a temperature of 0°C.

The transient temperature is calculated by (see Note S5 and Table S4 for details)

CellPress
OPEN ACCESS

Cell Reports
Physical Science
Report
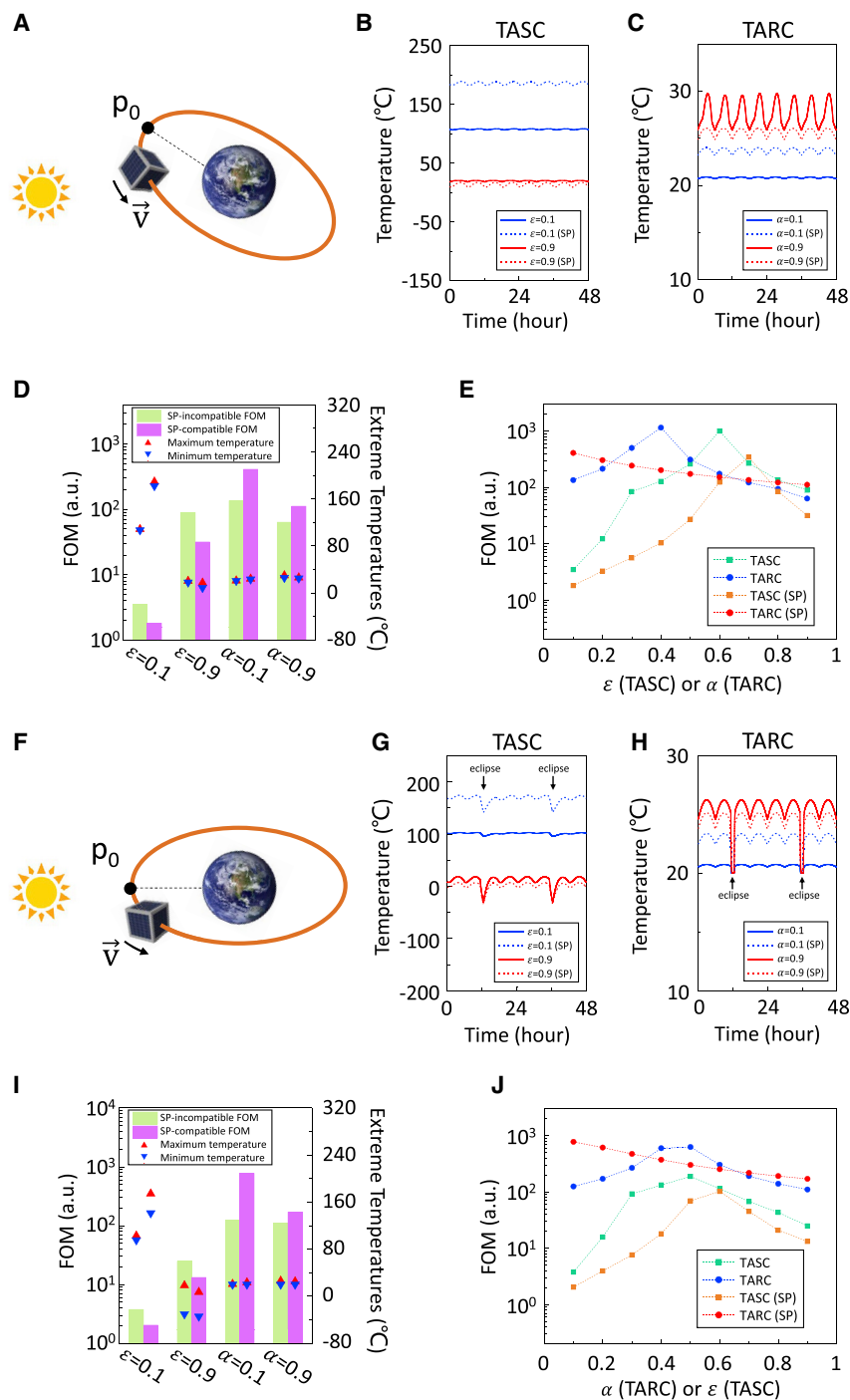
Figure 3. Transient thermal analysis of a 1U-CubeSat covered by TASCs or TARCs

(A) A schematic diagram of the geostationary CubeSat model when the Earth is at the December solstice.

(B and C) Transient temperatures of the CubeSat covered by TASCs or TARCs.

(D) Extracted FOMs and extreme temperatures for the cases in (B) and (C).

(E) FOMs as functions of static ε (or α) for TASCs (or TARCs) for the orbit in (A).

(F) A schematic diagram of the geosynchronous CubeSat model in the ecliptic plane.

(G and H) Transient temperatures of the CubeSat covered by TASCs or TARCs.

(I) Extracted FOMs and extreme temperatures for the cases in (G) and (H).

(J) FOMs as functions of static ε (or α) for TASCs or TARCs for the orbit in (F).

Cell Reports
Physical Science
Report

CellPress
OPEN ACCESS

$$Q_{Sun}(T, t) + Q_{Heat} + Q_{Albedo}(T, t) + Q_{ETR}(T, t) - Q_{TR}(T, t) = m \times c \times \frac{dT}{dt}.$$

(Equation 4)

As shown in Figure 1D, apart from direct solar heating and thermal radiative cooling, the temperature of Earth-orbiting satellites also depends on the heating from the sunlight reflected by the Earth (known as albedo) as well as thermal infrared (IR) radiation emitted from Earth, both of which can be regulated by temperature-adaptive coatings.

The transient temperatures of the CubeSats covered by different TASCs or TARCs are depicted in Figures 3B and 3C, respectively. The results show that the performance of TARCs in regulating the temperature around T_{set} is less sensitive to the value of the static α, while an unoptimized static ε can severely increase the temperature swing of a CubeSat covered by TASCs. Here, a static α or ε means the α or ε does not change with temperature. Furthermore, the SP compatibility deteriorates the temperature-regulation performance of TASCs due to the uncontrolled solar absorptivity in 0.4–1.1 μm, while SP-compatible TARCs behave well even with SP compatibility. The FOMs and extreme temperatures in Figure 3D also verify the above conclusions. Note that the FOM here is calculated by Equation 5 using the temperature data over an orbital period:

$$FOM = \frac{T_{set} \times \int_{period} dt}{\int_{period} |T(\theta) - T_{set}| dt}.$$

(Equation 5)

However, as plotted in Figure 3E, it is revealed that an optimized TASC ($\varepsilon = 0.6$) and an optimized TARC ($\alpha = 0.4$) could have comparable FOMs. The additional advantage of TASCs in this case comes from two aspects: (1) Earth albedo increases the amount of heat flux regulated by TASCs, and (2) Earth thermal IR radiation decreases the cooling efficiency of TARCs.

The above analyses are based on the absence of solar eclipse. Here, we also simulated the scenario where the 1U-CubeSat operates in the geosynchronous orbit in the ecliptic plane (Figure 3F), namely, the plane that the satellite will experience a solar eclipse during each circulation around the Earth. The transient temperatures of the orbiting CubeSats covered by different TASCs or TARCs (Figures 3G and 3H) show that TARCs outperform TASCs in reducing temperature swing of spacecrafts in missions. Strikingly, the temperature swing of the CubeSat covered by the low-α (0.1) TARC is merely 0.7°C, even with the solar eclipse at ~12 and ~36 h. Similarly, an optimized α is necessary for the best performance of TARCs, and SP-compatible TARCs can still effectively stabilize the CubeSat temperature. The advantage of TARCs over TASCs in the presence of eclipse is verified by Figure 3J, where the FOM of an optimized TASC is 189, far lower than that of an optimized TARC (628). More results can be found in Note S6 and Figures S6 and S7.

In-depth comparison of TASCs and TARCs in Earth orbits
The transient temperature simulation with and without solar eclipses leads to the comparison between TASCs and TARCs in Earth orbits: (1) for space missions without solar eclipses, optimized TASCs and TARCs have similar performance in reducing temperature swings; (2) when the space objects are subject to eclipses, TARCs are favorable due to their capacity of temperature regulation in the absence of solar light; (3) when used on SPs, TARCs perform better than TASCs; and (4) in-depth comparison between TASCs and TARCs involves detailed information about the space missions, including the planet thermal IR radiation flux, solar light flux, etc.

This is especially important for deep-space missions. For example, space objects in near-Venus orbits may receive much more solar irradiance and thermal IR radiation from Venus, which adds to the advantage of TASCs. As for near-Earth space objects, however, TARCs are more versatile. Moreover, the SP compatibility is technically more feasible with TARCs. As such, in the next part, we conduct an extensive investigation of transient temperatures of space objects covered by TARCs.

The previous model in Figure 3 only simulates the homogeneous temperature of a CubeSat by assuming that the entire CubeSat reaches thermal equilibrium instantaneously, with no consideration of the internal thermal resistance and resultant temperature inhomogeneity. To account for the temperature evolution of interior components and surfaces, we use a thermal model of CubeSat decomposed into seven nodes. As shown in Figure 4A, nodes #1–#6 are the six surfaces, while node #7 represents all the core components (electronics, battery, etc.) inside the satellite (details in Note S7 and Figure S8). The heat transfer among the seven nodes is calculated by

$$Q_i(t) = \begin{cases} \dfrac{T_7(t) - T_i(t)}{R_i}, & i < 7 \\ \displaystyle\sum_{j=1}^{6} \dfrac{T_j(t) - T_7(t)}{R_j}, & i = 7 \end{cases}, \qquad \text{(Equation 6)}$$

where Q, T, t, and R are the heat transfer power, temperature, time, and thermal resistance, respectively. The initial conditions are the same as those for Figure 3.

As shown in Figures 4B and 4C, the interior components of the CubeSat are effectively protected from temperature swings by a real-TARC: the temperature swing is only 2.6°C in an orbital period of the CubeSat. As a comparison, when the two non-switching references are used (see Table S3 for details), the temperature of node #7 goes extreme, fluctuating by 15.9°C or more around a baseline temperature as high as 79°C or as low as −30°C. The FOM for the real-TARC is 107.3–136.2 times higher than those of the references, and the influence of solar eclipses is negligible with real-TARC. If the CubeSat is completely covered by SPs and SP-compatible coatings, real-TARC can still restrict the temperature swing down to the range of 20.3°C–25.6°C, far lower than those of interior satellite components in some real space missions (Table S2). In Figure 4D, we plotted the FOMs and the temperature swings of all six exterior surfaces where SP-compatible coatings are used. With SP-compatible real-TARC equipped, the surface temperatures stay within 19.5°C–28.7°C, thus efficiently protecting the satellite structures from thermal fatigue damages. Since SPs may benefit from lower temperatures for a higher PV efficiency,[43] an ideal thermal design could simultaneously have room temperature interior components and low-temperature exterior SPs, which can be achieved by decreasing the T_{set} of TARC while optimizing the thermal resistances of the satellite (Note S8; Figures S9 and S10).

TARCs can be realized by phase-change materials (PCMs) such as vanadium dioxide, whose thermal IR properties undergo a reversible, fast, and drastic change upon temperature change crossing its phase-change temperature.[44–47] The target temperature T_{set} is set by the phase-change temperature of PCMs, which can be engineered by doping,[48] strain engineering,[49] etc. Desired ε and α of TASCs and TARCs can be engineered and tuned using artificial photonic structures, respectively.[22,27,50] Two existing challenges in this field are (1) TARCs were only experimentally demonstrated very recently, and existing designs have not been tested in space conditions,[22] and (2) the realization of SP-compatible TASCs and TARCs is an extremely ambitious and challenging task that requires groundbreaking photonic
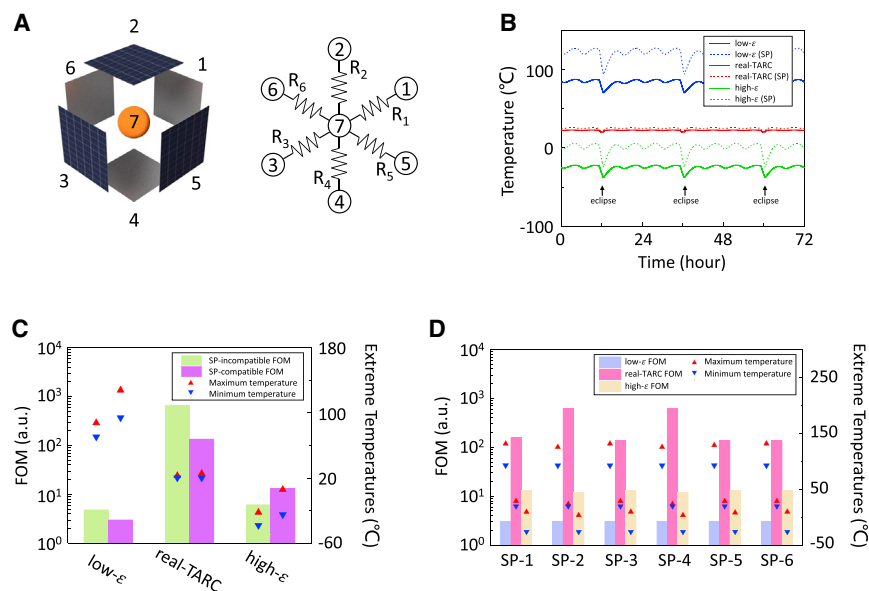
Figure 4. In-depth thermal analysis of solar panels and interior components of a geosynchronous CubeSat covered by TARC in the ecliptic plane
(A) An exploded diagram of the CubeSat (left) and the corresponding thermal resistance circuit (right).
(B) Transient temperatures of node #7.
(C) Extracted FOMs and extreme temperatures of node #7.
(D) Extracted FOMs and extreme temperatures of nodes #1–#6.

design and material engineering. Experimental realization of a functional TASC with a large α tuning range is yet to be demonstrated. Experimental implementation of TASCs and TARCs in space is yet to be achieved.

In conclusion, we systematically and theoretically analyzed the temperature-management performance of TASCs or TARCs for three thermal system models in outer space, eight TASCs or TARCs with different technical parameters, and one case study using data of experimentally realized TARCs. It is found that, though both TASCs and TARCs significantly stabilize the temperature of space objects, TARCs perform significantly better than TASCs due to the broad spectral range for thermal radiation in space, as well as larger physical surface area for thermal emission than for solar absorption. Furthermore, when the temperature-adaptive coatings are designed to be spectrally compatible to SPs, they (especially TARCs) bring great advantages in temperature management without sacrificing the solar power generation of space objects. As a result, thin, light-weight, and cost-effective TARCs show great promise as the future passive TMT for space missions with exceptional temperature-stabilization capabilities.

EXPERIMENTAL PROCEDURES

Resource availability

Lead contact

Further information and requests for resources and materials should be directed to and will be fulfilled by the lead contact, Junqiao Wu (wuj@berkeley.edu).

Materials availability

This study did not generate new unique reagents.

Data and code availability

The data presented in this work are available from the lead contact upon reasonable request.

SUPPLEMENTAL INFORMATION

Supplemental information can be found online at https://doi.org/10.1016/j.xcrp.2022.101066.

AUTHOR CONTRIBUTIONS

K.D. and J.W. conceived the idea. K.D., D.T., J.L., S.W., and J.Y. conducted the modeling and simulation. K.D. wrote the manuscript with assistance from other authors. All authors reviewed and revised the manuscript.

DECLARATION OF INTERESTS

The authors declare no competing interests.

REFERENCES

1. J.D. Cressler, and H.A. Mantooth, eds. (2017). Extreme environment electronics (CRC Press). https://www.routledge.com/Extreme-Environment-Electronics/Cressler-Mantooth/p/book/9781138074224.

2. Pisacane, V.L. (2003). Spacecraft systems design and engineering. In Encyclopedia of Physical Science and Technology, 3rd ed., R.A. Meyers, ed. (Elsevier Science Ltd), pp. 464–483. https://doi.org/10.1016/B0-12-227410-5/00888-7.

3. Karam, R.D. (1998). Satellite thermal control for systems engineers (Vol. 181). In Progress in Astronautics and Aeronautics, P. Zarchan, ed. (Aiaa). https://doi.org/10.2514/4.866524.

4. Thirsk, R., Kuipers, A., Mukai, C., and Williams, D. (2009). The space-flight environment: the international space station and beyond. CMAJ (Can. Med. Assoc. J.) 180, 1216–1220. https://doi.org/10.1503/cmaj.081125.

5. Toropova, M.M. (2021). Thermally adaptive axisymmetric trusses for satellite platforms. Acta Astronaut. 181, 139–150. https://doi.org/10.1016/j.actaastro.2021.01.014.

6. Asmar, S.W., Armstrong, J.W., Iess, L., and Tortora, P. (2005). Spacecraft Doppler tracking: noise budget and accuracy achievable in precision radio science observations. Radio Sci. 40, 1–9. https://doi.org/10.1029/2004RS003101.

7. Delabrouille, J. (1998). Analysis of the accuracy of a destriping method for future cosmic microwave background mapping with the PLANCK SURVEYOR satellite. Astron.

Astrophys., Suppl. Ser. 127, 555–567. https://doi.org/10.1051/aas:1998119.

8. Pippin, G. (2003). Space environments and induced damage mechanisms in materials. Prog. Org. Coat. 47, 424–431. https://doi.org/10.1016/j.porgcoat.2003.07.003.

9. Hengeveld, D., Mathison, M., Braun, J., Groll, E., and Williams, A. (2010). Review of modern spacecraft thermal control technologies. HVAC R Res. 16, 189–220. https://doi.org/10.1080/10789669.2010.10390900.

10. (2022). 7.0 Thermal Control (National Aeronautics and Space Administration). https://www.nasa.gov/smallsat-institute/sst-soa/thermal-control.

11. He, Y., Li, B., Wang, Z., and Zhang, Y. (2021). Thermal design and verification of spherical scientific satellite Q-SAT. International Journal of Aerospace Engineering, 1–11. https://doi.org/10.1155/2021/9961432.

12. Bhatt, J.H., and Barve, J.J. (2019). Control of spaceborne linear cryocoolers: a review. Prog. Aero. Sci. 109, 100544. https://doi.org/10.1016/j.paerosci.2019.05.004.

13. Guo, D., Sheng, Q., Dou, X., Wang, Z., Xie, L., and Yang, B. (2020). Application of thermoelectric cooler in temperature control system of space science experiment. Appl. Therm. Eng. 168, 114888. https://doi.org/10.1016/j.applthermaleng.2019.114888.

14. Sunada, E., Bhandari, P., Carroll, B., Hendricks, T., Furst, B., Kempenaar, J., et al. (2016). A two-

phase mechanically pumped fluid loop for thermal control of deep space science missions. In 46th International Conference on Environmental Systems. https://ttu-ir.tdl.org/handle/2346/67545.

15. Liu, T., Sun, Q., Meng, J., Pan, Z., and Tang, Y. (2016). Degradation modeling of satellite thermal control coatings in a low earth orbit environment. Sol. Energy 139, 467–474. https://doi.org/10.1016/j.solener.2016.10.031.

16. Baturkin, V. (2005). Micro-satellites thermal control—concepts and components. Acta Astronaut. 56, 161–170. https://doi.org/10.1016/j.actaastro.2004.09.003.

17. Kim, Y.S., Lee, E.S., and Woo, S.H. (2003). System trade-off study and opto-thermo-mechanical analysis of a sunshield on the MSC of the KOMPSAT-2. Journal of Astronomy and Space Sciences 20, 393–402. https://doi.org/10.5140/JASS.2003.20.4.393.

18. Evans, A.L. (2019, August). Design and testing of the CubeSat form factor thermal control louvers. In 33rd Annual AIAA/USU Conference on Small Satellites. https://ntrs.nasa.gov/citations/20190028943.

19. Bacciotti, A., Bucchi, F., Frendo, F., Mameli, M., Perna, R., and Filippeschi, S. (2021, February). On the use of shape memory alloys for deployable passive heat radiators in space satellites. IOP Conf. Ser. Mater. Sci. Eng. 1038, 012061. https://doi.org/10.1088/1757-899X/1038/1/012061.

Cell Reports
Physical Science
Report

20. Heo, H., Li, S., Bao, H., and Ju, J. (2019). A passive thermal switch with kirigami-inspired mesostructures. Adv. Eng. Mater. 21, 1900225. https://doi.org/10.1002/adem.201900225.

21. Farid, M.M., Khudhair, A.M., Razack, S.A.K., and Al-Hallaj, S. (2004). A review on phase change energy storage: materials and applications. Energy Convers. Manag. 45, 1597–1615. https://doi.org/10.1016/j.enconman.2003.09.015.

22. Tang, K., Dong, K., Li, J., Gordon, M.P., Reichertz, F.G., Kim, H., Rho, Y., Wang, Q., Lin, C.Y., Grigoropoulos, C.P., et al. (2021). Temperature-adaptive radiative coating for all-season household thermal regulation. Science 374, 1504–1509. https://doi.org/10.1126/science.abf7136.

23. Ono, M., Chen, K., Li, W., and Fan, S. (2018). Self-adaptive radiative cooling based on phase change materials. Opt Express 26, A777–A787. https://doi.org/10.1364/OE.26.00A777.

24. Hippalgaonkar, K. (2022). All-weather thermal regulation coatings. Joule 6, 286–288. https://doi.org/10.1016/j.joule.2022.01.012.

25. Kim, H., Cheung, K., Auyeung, R.C.Y., Wilson, D.E., Charipar, K.M., Piqué, A., and Charipar, N.A. (2019). VO₂-based switchable radiator for spacecraft thermal control. Sci. Rep. 9, 11329–11338. https://doi.org/10.1038/s41598-019-47572-z.

26. Sun, K., Xiao, W., Wheeler, C., Simeoni, M., Urbani, A., Gaspari, M., et al. (2022). VO₂ metasurface smart thermal emitter with high visual transparency for passive radiative cooling regulation in space and terrestrial applications. Nanophotonics. https://doi.org/10.1515/nanoph-2022-0020.

27. Sun, K., Riedel, C.A., Urbani, A., Simeoni, M., Mengali, S., Zalkovskij, M., Bilenberg, B., de Groot, C., and Muskens, O.L. (2018). VO₂ thermochromic metamaterial-based smart optical solar reflector. ACS Photonics 5, 2280–2286. https://doi.org/10.1021/acsphotonics.8b00119.

28. Xu, X., Gu, J., Zhao, H., Zhang, X., Dou, S., Li, Y., Zhao, J., Zhan, Y., and Li, X. (2022). Passive and dynamic phase-change-based radiative cooling in outdoor weather. ACS Appl. Mater. Interfaces 14, 14313–14320. https://doi.org/10.1021/acsami.1c23401.

29. Villela, T., Costa, C.A., Brandão, A.M., Bueno, F.T., and Leonardi, R. (2019). Towards the thousandth CubeSat: a statistical overview. International Journal of Aerospace Engineering, 1–13. https://doi.org/10.1155/2019/5063145.

30. Amores, A.P., Ravishankar, A.P., and Anand, S. (2022, April). Design and modelling of metal-oxide nanodisk arrays for structural colors and UV-blocking functions in solar cell glass covers. Photonics 9, 273. https://doi.org/10.3390/photonics9050273.

31. Vitanov, P., Delibasheva, M., Goranova, E., and Peneva, M. (2000). The influence of porous silicon coating on silicon solar cells with different emitter thicknesses. Sol. Energy Mater. Sol. Cells 61, 213–221. https://doi.org/10.1016/S0927-0248(99)00110-5.

32. Yao, Y., Wang, L., Zhu, X., Tu, W., Zhou, Y., Liu, R., Sun, J., Tao, B., Wang, C., Yu, X., et al. (2022). Extraterrestrial photosynthesis by Chang'E-5 lunar soil. Joule 6, 1008–1014. https://doi.org/10.1016/j.joule.2022.04.011.

33. The national renewable energy laboratory (2022). Solar Spectra. https://www.nrel.gov/grid/solar-resource/spectra.html.

34. Chen, Z., Zhu, L., Li, W., and Fan, S. (2019). Simultaneously and synergistically harvest energy from the sun and outer space. Joule 3, 101–110. https://doi.org/10.1016/j.joule.2018.10.009.

35. Chin, A., Coelho, R., Nugent, R., Munakata, R., and Puig-Suari, J. (2008, September). CubeSat: the pico-satellite standard for research and education. In AIAA Space 2008 Conference & Exposition, p. 7734. https://doi.org/10.2514/6.2008-7734.

36. Lincot, D. (2017). The new paradigm of photovoltaics: from powering satellites to powering humanity. C. R. Phys. 18, 381–390. https://doi.org/10.1016/j.crhy.2017.09.003.

37. Zampiva, R.Y., Kaufmann, C.G., Jr., Acauan, L.H., Seeger, R.L., Bonatto, F., Boeira, C.D., Santos, W.Q., Jacinto, C., Figueroa, C.A., Dorneles, L.S., et al. (2018). Luminescent anti-reflection coatings based on Er³⁺ doped forsterite for commercial silicon solar cells applications. Sol. Energy 170, 752–761. https://doi.org/10.1016/j.solener.2018.05.097.

38. Garzón, A., and Villanueva, Y.A. (2018). Thermal analysis of satellite libertad 2: a guide to cubesat temperature prediction. J. Aerosp. Technol. Manag. 10, E4918. https://doi.org/10.5028/jatm.v10.1011.

39. Morsch Filho, E., Nicolau, V.d.P., Paiva, K.V.d., and Possamai, T.S. (2020). A comprehensive attitude formulation with spin for numerical model of irradiance for CubeSats and Picosats. Appl. Therm. Eng. 168, 114859. https://doi.org/10.1016/j.applthermaleng.2019.114859.

40. Vega Martinez, S., Filho, E.M., Seman, L.O., Bezerra, E.A., Nicolau, V.D.P., Ovejero, R.G., and Leithardt, V.R.Q. (2021). An integrated thermal-electrical model for simulations of battery behavior in CubeSats. Appl. Sci. 11, 1554. https://doi.org/10.3390/app11041554.

41. Hernández-Gómez, J.J., Yañez-Casas, G.A., Torres-Lara, A.M., Couder-Castañeda, C., Orozco-del-Castillo, M.G., Valdiviezo-Navarro, J.C., Medina, I., Solís-Santomé, A., Vázquez-Álvarez, D., and Chávez-López, P.I. (2019, November). Conceptual low-cost on-board high performance computing in CubeSat nanosatellites for pattern recognition in Earth's remote sensing. Proceedings of the 1st International Conference on Geospatial Information Sciences 13, 114–122. https://doi.org/10.29007/8d25.

42. CanX-7 (Canadian Advanced Nanospace eXperiment-7) (2022). ESA Earth Observation Portal. https://directory.eoportal.org/web/eoportal/satellite-missions/c-missions/canx-7.

43. Fesharaki, V.J., Dehghani, M., Fesharaki, J.J., and Tavasoli, H. (2011). The effect of temperature on photovoltaic cell efficiency. In Proceedings of the 1st International Conference on Emerging Trends in Energy Conservation–ETEC, Tehran, Iran, pp. 20–21. https://research.iaun.ac.ir/pd/jjfesharakiold/pdfs/PaperC_4124.pdf.

44. Dong, K., Hong, S., Deng, Y., Ma, H., Li, J., Wang, X., Yeo, J., Wang, L., Lou, S., Tom, K.B., et al. (2018). A lithography-free and field-programmable photonic metacanvas. Adv. Mater. 30, 1703878. https://doi.org/10.1002/adma.201703878.

45. Kats, M.A., Sharma, D., Lin, J., Genevet, P., Blanchard, R., Yang, Z., Qazilbash, M.M., Basov, D.N., Ramanathan, S., and Capasso, F. (2012). Ultra-thin perfect absorber employing a tunable phase change material. Appl. Phys. Lett. 101, 221101. https://doi.org/10.1063/1.4767646.

46. Wang, S., Jiang, T., Meng, Y., Yang, R., Tan, G., and Long, Y. (2021). Scalable thermochromic smart windows with passive radiative cooling regulation. Science 374, 1501–1504. https://doi.org/10.1126/science.abg0291.

47. Ke, Y., Yin, Y., Zhang, Q., Tan, Y., Hu, P., Wang, S., Tang, Y., Zhou, Y., Wen, X., Wu, S., et al. (2019). Adaptive thermochromic windows from active plasmonic elastomers. Joule 3, 858–871. https://doi.org/10.1016/j.joule.2018.12.024.

48. Tang, K., Dong, K., Nicolai, C.J., Li, Y., Li, J., Lou, S., Qiu, C.W., Raulet, D.H., Yao, J., and Wu, J. (2020). Millikelvin-resolved ambient thermography. Sci. Adv. 6, eabd8688. https://doi.org/10.1126/sciadv.abd8688.

49. Howard, S.A., Evlyukhin, E., Páez Fajardo, G., Paik, H., Schlom, D.G., and Piper, L.F.J. (2021). Digital tuning of the transition temperature of epitaxial VO₂ thin films on MgF₂ substrates by strain engineering. Adv. Mater. Interfaces 8, 2001790. https://doi.org/10.1002/admi.202001790.

50. Long, L., Taylor, S., and Wang, L. (2020). Enhanced infrared emission by thermally switching the excitation of magnetic polariton with scalable microstructured VO₂ metasurfaces. ACS Photonics 7, 2219–2227. https://doi.org/10.1021/acsphotonics.0c00760.

Supplemental information

Reducing temperature swing

of space objects with temperature-adaptive

solar or radiative coating

Kaichen Dong, Derick Tseng, Jiachen Li, Sorren Warkander, Jie Yao, and Junqiao Wu

Note S1. Temperature Swings of Space Objects and Temperature Management Technologies (TMTs)

The temperature of space objects is dependent on many factors, especially for the objects in the solar system. For example, an Earth satellite receives solar heating from the Sun and Earth albedo, thermal radiative heating from Earth and the space background, while it strongly emits heat into outer space via thermal radiation. If TMTs are not properly installed, the uncontrolled temperatures of exterior surfaces can easily swing between -220 ℃ and +220 ℃.[1] On the other hand, all spacecraft components have their own operating temperatures and survival temperatures,[1] with examples shown in Table S1.

Table S1. Representative operating temperature ranges of spacecraft components[1-4]

Component	Operating temperature (℃)
batteries	-5 to +85
antennas	-40 to +85
solar panels	-100 to +150
cameras	-40 to +85
altitude determination and control systems	-30 to +85
on-board computers	-40 to +85
mechanical structures	-100 to +100

Though those components are designed with large operating temperature ranges to survive the extreme thermal conditions in space, it is desired to regulate their temperatures with high thermal stability, which helps reduce the thermal fatigue of mechanical structures,[4] decrease the instrumental misalignment,[5] and minimize the noise induced by thermal fluctuation.[6] To suppress the temperature fluctuations, advanced TMTs are applied to spacecrafts. Representative temperature swings of spacecraft components are listed in Table S2.

Table S2. Measured or predicted temperature swings and corresponding TMTs of representative spacecraft components (* indicates predicted temperature results by thermal analysis)

Spacecraft	Component	Temperature swing (℃)	On-board TMT(s)	Reference
International Space Station (ISS)	crew compartment	+21 to +23	deployable radiators, heaters, fluid pumps, etc.	7,8
	external surface	-100 to +100		
Dynamic Ionosphere CubeSat	battery	+5 to +14	heaters, thermal shields (isolated solar panels), etc.	9
	external side	-35 to +35		
MinXSS 3U CubeSat	battery	+10 to +16 (cold case) +17 to +21 (hot case)	heaters, radiators, etc.	10
	+X solar array	-10 to +55 (cold case) +58 to +61 (hot case)		

Amazonia-1 Satellite*	battery	-8 to +16	coatings, radiators, heaters, etc.	11
	star sensor	-12 to +42		
Resourcesat-2	electro-optics module of camera	+17 to +23	heaters, etc.	12
	CCD module	+18 to +22		
TURKSAT-3USAT	camera card	-60 to +73	heaters, multilayer insulation, etc.	2
	transponder	-28 to +65		
SPEQTRE CubeSat*	on-board computer	-32 to +21	radiators, etc.	13
	mechanical structure	-37 to +34		
	optical payload	-28 to +10		
UWE-1	battery	+16 to +23	thermal isolation, etc.	14
	solar panel	+11 to +30		
Luojia 1-01	star tracker	+12 to +15	multilayer heat insulation assembly, heat conductivity grease/membrane, coatings, etc.	15
	camera	+15 to +23		
	digital sun sensor	+10 to +22		

Table S2 clearly shows that, the temperature swing ranges of spacecraft components are mostly ranging from several Celsius degrees to tens of Celsius degrees around ~20 ℃. Exterior components may have larger temperature swings due to the strong thermal interaction with the space environment. Passive TMTs are essential but active TMTs are more effective in maintaining a small temperature swing. Some miniature satellites (for example, CubeSats) may suffer from large temperature swings due to the lack of power and space for advanced active TMTs.

Note S2. Properties of the Coatings Used in This Work

(1) Temperature-adaptive solar coatings (TASCs) and temperature-adaptive radiative coatings (TARCs) without solar panel compatibility

In this work, the temperature-regulation performance of TASCs and TARCs are simulated and compared. To properly analyze their performance, the temperature-adaptive solar absorptivity (α) of TASCs are assigned with an optimal tuning range of 0.1-0.9. To stabilize the temperature, solar heating should be maximized only at lower temperatures. The transition temperature range of 19 ℃ to 27 ℃ is taken from previous work.[16] Therefore, $\alpha(T)$ of TASCs in our work without solar panel (SP) compatibility is (left inset of Figure 1A in the main text):

$$\alpha(T) = \begin{cases} 0.9, & T \leq 19℃ \\ 0.1, & T \geq 27℃ \end{cases} \qquad \text{Equation S1}$$

where T is the temperature of TASCs. Between 19 ℃ and 27 ℃, we assume that $\alpha(T)$ changes linearly with T. Meanwhile, the thermal emissivity (ε) of TASCs is static and independent of temperature. To properly assess the influence of ε on the performance of TASCs, we simulated two TASCs with ε=0.1 and ε=0.9, respectively.

Similarly, $\varepsilon(T)$ of TARCs in our work is defined by Equation S2 so that TARCs dissipate more heat at higher temperatures (right inset of Figure 1A in the main text).

$$\varepsilon(T) = \begin{cases} 0.1, & T \leq 19°C \\ 0.9, & T \geq 27°C \end{cases} \qquad \text{Equation S2}$$

The $\varepsilon(T)$ is assumed to linearly change with temperature within the 19 ℃ to 27 ℃ range. Two TARCs are simulated with α=0.1 and α=0.9, respectively.

Besides, all SP-incompatible TASCs and TARCs have 0% transmission in both solar and thermal spectra:

$$\alpha + r = 1 \qquad \text{Equation S3}$$

where r is the reflectivity of TASCs and TARCs.

(2) TASCs and TARCs with solar panel compatibility

Another important component of spacecrafts that needs temperature management is solar panels (SPs), whose temperature may strongly increase under solar irradiation and drop during solar eclipses.[17,18] Such gigantic temperature swings may cause thermal stress and thermally induced vibrations in SPs.[17,18] If TASCs or TARCs can be used to regulate the temperature of those SPs, the above problems may be solved. Moreover, miniature satellites usually have body-mounted SPs.[19] To use TASCs or TARCs on those miniature satellites, it is necessary to ensure SP-compatibility because the SPs are essential and cannot be replaced by SP-incompatible TASCs or TARCs.

When TASCs or TARCs are installed on SPs (Figure S1A), solar light passes through TASCs or TARCs before entering the SPs. To ensure that the majority of solar energy within the SP responsibility range arrives at SP, SP-compatible TASCs should have a 100% transmission band from 0.4 μm to 1.1 μm,[20,21] as illustrated in Figure S1. Similarly, the α of SP-compatible TARCs (including real-TARC and its two references in the Figure 4 of the main text) also has such a 100% transmission band.
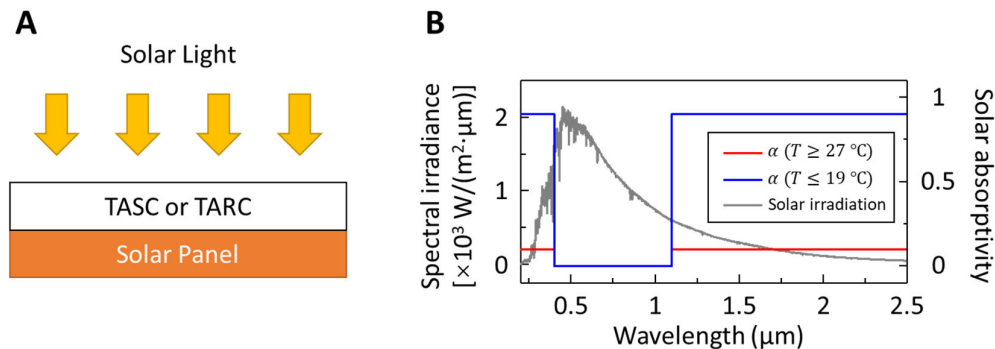
Figure S1. Installation of TASCs or TARCs on SPs

(A) Schematic configuration where TASC or TARC is applied on a SP.

(B) Spectrum of AM0 solar irradiance and temperature-adaptive solar absorptivity (α) of SP-compatible TASCs.

Herein, SP-compatible TASCs and TARCs can be described by

$$\begin{cases} \alpha + r = 1, & \lambda < 0.4\ \mu m \text{ or } \lambda > 1.1\ \mu m \\ t_T = 1, & 0.4\ \mu m \leq \lambda \leq 1.1\ \mu m \end{cases} \qquad \text{Equation S4}$$

where t_T is transmissivity and λ is wavelength.

The reflectivity (r_{SP}) and photovoltaic efficiency (η_{SP}) of SP in this work is 0.1 and 0.25, respectively.[22-24] The heating coefficient (α_{SP}) of SPs is thus calculated by

$$\alpha_{SP} + \eta_{SP} + r_{SP} = 1 \qquad \text{Equation S5}$$

Nevertheless, it is important to point out that for solar array wings, TASCs and TARCs can be applied onto the back surface of SPs.[25] As a result, the 100% transmission band in 0.4-1.1 μm is not necessary for SP-compatibility in such a scenario. In this paper, the SP-compatibility only refers to the scenario where TASCs and TARCs are used on the front surface of SPs.

As a conclusion, the α and ε of all materials, both SP-compatible and SP-incompatible, are listed in Table S3.

Table S3. Solar absorptivity and thermal emissivity of coatings used in our simulation

Coatings		Temperature (℃)	Solar absorptivity		Thermal emissivity
			out of 0.4-1.1 μm	0.4-1.1 μm	
TASC	ε=0.1	≤19	0.9		0.1
		≥27	0.1		
	ε=0.1 (SP)	≤19	0.9	0	0.1
		≥27	0.1		
	ε=0.9	≤19	0.9		0.9
		≥27	0.1		
	ε=0.9 (SP)	≤19	0.9	0	0.9
		≥27	0.1		
TARC	α=0.1	≤19	0.1		0.1
		≥27			0.9
	α=0.1 (SP)	≤19	0.1	0	0.1
		≥27			0.9
	α=0.9	≤19	0.9		0.1
		≥27			0.9
	α=0.9 (SP)	≤19	0.9	0	0.1
		≥27			0.9
real-TARC		≤19	0.25		0.17
		≥27			0.72
real-TARC (SP)		≤19	0.25	0	0.17
		≥27			0.72
low-ε		≤19	0.25		0.17
		≥27			

low-ε (SP)	≤19	0.25	0	0.17
	≥27			
high-ε	≤19	0.25		0.72
	≥27			
high-ε (SP)	≤19	0.25	0	0.72
	≥27			

Note S3. Supplemental Thermal Analysis for the Two-Dimensional (2D) Board Model

(1) The influence of the surface temperature when $\theta=0°$

In the main text, the 2D board model is analyzed without the case where the solar altitude angle $\theta=0°$, because the surface temperature always equals to the space temperature of 2.7 K [26] at $\theta=0°$, regardless of the surface α and ε. With the temperature data at $\theta=0°$, the plots are shown in Figure S2.
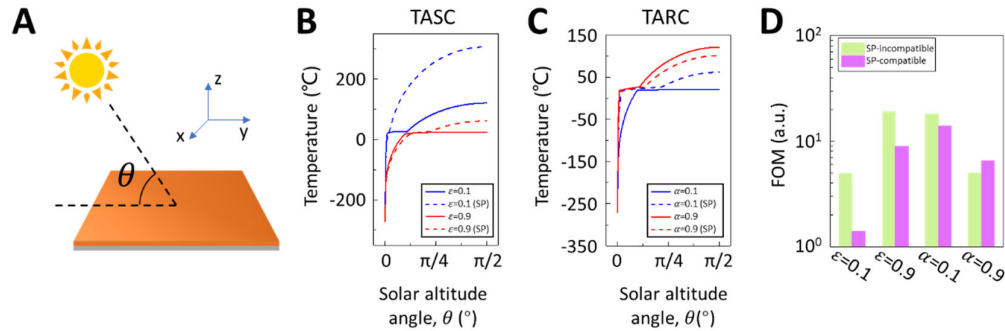

Figure S2. Thermal analysis of the 2D board model with $\theta=0°$ data

(A) A schematic diagram of the 2D board model.

(B and C) Static surface temperatures as functions of θ for boards covered by TASCs or TARCs. Note that SP represents SP-compatibility.

(D) Extracted figures of merit (FOMs) for the cases in (B) and (C).

(2) The respective influence of ε and α on the FOMs for TASCs and TARCs

In the main text, we only compared TASCs and TARCs with static ε and α of 0.1 and 0.9, respectively. Here we performed the simulation with more static ε and α for TASCs and TARCs, respectively, and plotted the FOMs as functions of static ε or α in Figure S3.
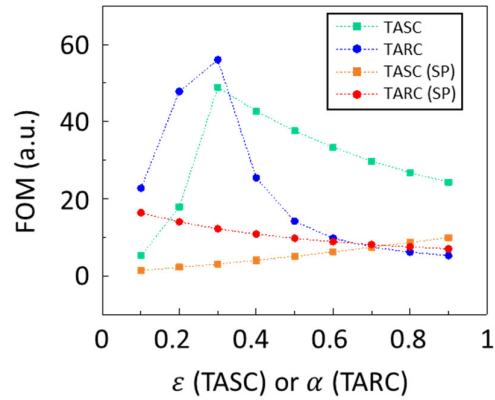
Figure S3. FOMs as functions of static ε and α for TASCs and TARCs, respectively.

Figure S3 shows that an optimized static ε or α exists for TASCs or TARCs. Future design of TASCs or TARCs should consider the optimization of static ε or α for optimal performance. The difference between SP-incompatible and SP-compatible cases lies in the 100% transmission band of 0.4-1.1 µm, where 65% of the total solar energy is converted to heat by the underneath SPs. For the SP-compatible TASCs, the limited temperature-adaptive α severely deteriorates their performance. On the other hand, the effective static α of SP-compatible TARCs is subject to the uncontrolled α_{SP}=65% in the wavelength range of 0.4-1.1 µm, so the FOM of SP-compatible TARCs cannot be optimized to the optimal value.

Note S4. Supplemental Thermal Analysis for the Three-Dimensional (3D) Cube Model

In the main text, the 3D cube model (Figure 2E) is used where the sunbeam direction is in the YZ-plane and normal to the -Y and +Z cube surfaces when θ=0° and $\pi/2$, respectively (Figure S4A and S4B). Here, to prove the validity of our conclusions in the main text, the cube is rotated clockwise by $\pi/4$ in the XY-plane (Figure S4C). In this simulation, the sunbeam is in the XY-plane and normal to +Z cube surface when θ=0° and $\pi/2$, respectively.
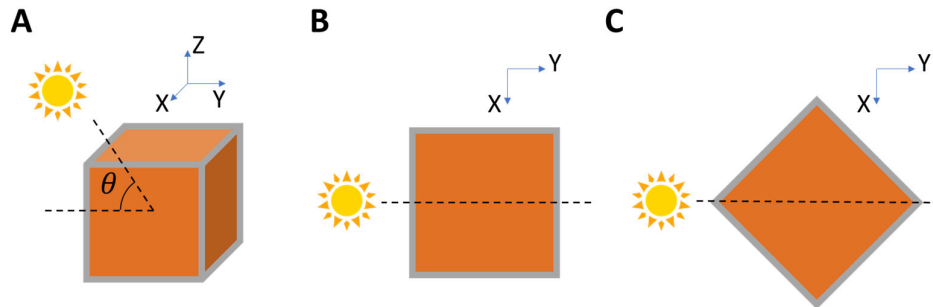

Figure S4. Schematic diagrams of the cube model
(A) A schematic diagram of the 3D cube model used in the main text.
(B and C) Top views of the model used in the main text (B) and the Supplemental Information (C).
Note that the dashed lines indicate the plane in which the sunbeam direction is.

The calculation results are shown in Figure S5. Note that the peak in Figure S5B is due to the strong solar heating power that overwhelms the cooling capacity of SP-incompatible TARC with α=0.9 above T=27 ℃. This result, together with Figure S5C, again proves the importance of optimizing static ε or α for TASCs or TARCs, respectively.
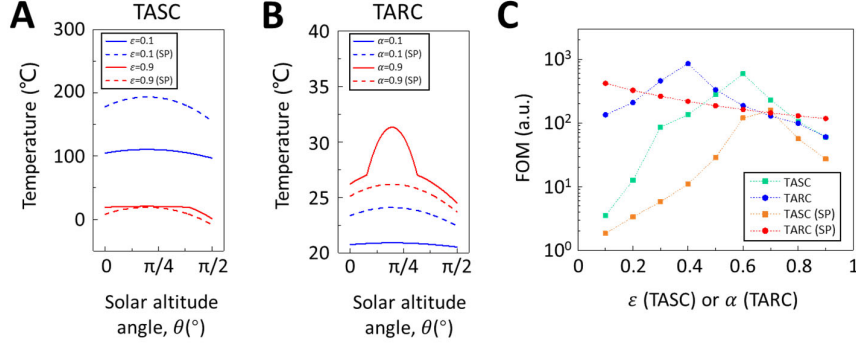
Figure S5. Supplemental thermal analysis results of the cube model

(A and B) Static surface temperatures as functions of θ for cubes covered by TASCs or TARCs, where SP represents SP-compatibility.

(C) Extracted FOMs for the cases in (A) and (B).

Note S5. Thermal Analysis Equations for the CubeSat Model

The thermal analysis of CubeSats in an Earth orbit has been conducted in previous works.[3,26,27] Here, our thermal analysis equations are described as follows:

In the CubeSat model used for Figure 3 in the main text, the thermal conductivity of the CubeSat is infinite, meaning that the temperature gradient within the CubeSat is zero everywhere. Such an ideal model helps avoid the formulation of heat exchanges between surfaces and the interior components of CubeSat, providing a fast and simplified thermal analysis of the CubeSat with a reasonable accuracy.[26]

The radiative heat exchange power (Q_{rad}) for the CubeSat as a function of CubeSat temperature (T) is defined as:

$$Q_{rad}(T,t) = Q_{Sun}(T,t) + Q_{Albedo}(T,t) + Q_{ETR}(T,t) - Q_{TR}(T,t) \qquad \text{Equation S6}$$

where Q_{Sun}, Q_{Albedo}, Q_{ETR}, Q_{TR} are the heat transfer power of solar irradiance (heating), Earth albedo (heating), thermal radiation of Earth (heating), and thermal radiation of the CubeSat (cooling), respectively. T and t are the temperature of CubeSat and time, respectively.

The major heating source of the CubeSat comes from solar irradiation, which is modeled by:

$$Q_{Sun}^{i}(T,t) = \alpha^{i}(T,t) \times I_{Sun} \times A^{i} \times F_{Sun}^{i}(t) \times \Delta(t) \qquad \text{Equation S7}$$

Here, $Q_{Sun}^{i}(T,t)$, $\alpha^{i}(T,t)$, A^{i} are the solar heating power, solar absorptivity, surface area of the CubeSat surface i, respectively. I_{Sun} is the solar irradiation power flux of 1367 W/m². $F_{Sun}^{i}(t)$ is the view factor of the surface i in relation to the Sun. $\Delta(t)$ is a step function, which is 1 if the CubeSat is exposed to the Sun, and 0 if the CubeSat is in a solar eclipse.

Another heating source is the reflected solar energy by the Earth: Solar irradiance arrives at the surface of the Earth first, get reflected, and absorbed by the CubeSat eventually, which can be simulated by:

$$Q_{Albedo}^i(T,t) = \alpha^i(T,t) \times R_{Earth} \times I_{Sun} \times A^i \times F_{Earth}^i(t) \times P(t) \qquad \text{Equation S8}$$

where $Q_{Albedo}^i(T,t)$ is the albedo radiation heating power of the CubeSat surface i, R_{Earth} is the albedo coefficient, and $F_{Earth}^i(t)$ is the view factor of the surface i in relation to the Earth. $P(t)$ is the term that models the Earth albedo as a specular source.[26]

The third heating source is the thermal infrared (IR) radiation from the Earth to the CubeSat:

$$Q_{ETR}^i(T,t) = \alpha_{IR}^i(T,t) \times H_{Earth} \times A^i \times F_{Earth}^i(t) \qquad \text{Equation S9}$$

where $Q_{ETR}^i(T,t)$ is the thermal IR radiation from the Earth to the CubeSat surface i, $\alpha_{IR}^i(T,t)$ is the thermal IR absorptivity of the CubeSat surface i, H_{Earth} is the total thermal IR radiation heat flux emitted by the Earth.

The last term in Equation S6, $Q_{TR}(T,t)$, is the thermal radiation cooling of the CubeSat, which can be calculated by:

$$Q_{TR}^i(T,t) = \varepsilon^i(T,t) \times A^i \times \sigma \times \left(T(t)^4 - T_{space}^4\right) \qquad \text{Equation S10}$$

In Equation S10, $Q_{TR}^i(T,t)$ and $\varepsilon^i(T,t)$ are the thermal radiation cooling power and thermal emissivity of the surface i, respectively. σ is the Stefan-Boltzmann constant. T_{space} is the temperature of the outer space background (2.7 K).

Note that for the SP-compatible cases, the solar energy heating power in and out of the 0.4-1.1 μm wavelength range is calculated separately.

Using the above equations, we can calculate the transient temperature of the CubeSat by:

$$Q_{rad}(T,t) + Q_{Heat} = m_{sat} \times c_{sat} \times \frac{dT}{dt} \qquad \text{Equation S11}$$

where Q_{Heat} is the heat generated by the interior components of the CubeSat; m_{sat} and c_{sat} are the mass and specific heat capacity of the CubeSat, respectively. The specific heat capacity of aluminum (c_{Al}) is 890 J/(kg·℃) and the c_{sat} is assumed to be the same as c_{Al}.

The parameters used in the simulation are listed in Table S4. Note that the CubeSat analyzed in this work is a 1U-CubeSat (10 cm×10 cm×10 cm).

Table S4. Parameters for the calculation of the CubeSat model

Parameter	Value	Meaning	Reference
A	0.01 m^2	physical area of one CubeSat surface	28-30
I_{Sun}	1367 W/m^2	solar irradiation heat flux	3,31
R_{Earth}	0.3	albedo coefficient of the Earth	27
H_{Earth}	237 W/m^2	thermal IR radiation flux of the Earth	27
σ	5.67×10^{-8} W/(m^2·K^4)	the Stefan-Boltzmann constant	N/A
T_{space}	2.7 K	space background temperature	26,27,32
m_{sat}	1 kg	total mass of the CubeSat	29,30
c_{sat}	890 J/(kg·℃)	specific heat capacity of the CubeSat	N/A
Q_{Heat}	5 W	heat generated by the interior components of the CubeSat	33,34

Note S6. Supplemental Thermal Analysis for a 1U-CubeSat Covered by TASCs or TARCs

(1) The transient temperature of a CubeSat covered by TASCs with a static ε=0.7

In the CubeSat model, SP-compatible TASCs suffer from the uncontrolled solar absorptance in the wavelength range of 0.4-1.1 μm, so their performance in reducing temperature swings is worse than the SP-incompatible TASCs. However, in Figure 3E of the main text, FOM of TASC (SP) is higher than that of TASC when ε=0.7, which is due to the fact that the FOM is evaluated by the target temperature T_{set}=23 ℃. The transient temperatures for the two cases are compared in Figure S6B.
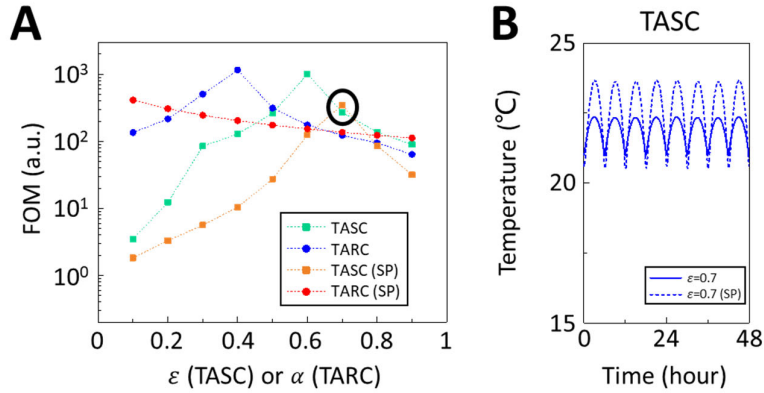
**Figure S6. Supplemental results for Figure 3E of the main text**
(A) FOMs as functions of static ε (or α) for TASCs (or TARCs) for the orbit in Figure 3A of the main text. The black circle indicates the cases for (B).
(B) Transient temperatures of a CubeSat covered by TASCs with a static ε=0.7.

Figure S6B clearly depicts that the temperature swing of TASC is much smaller than that of TASC (SP). So in terms of the temperature swing reduction, TASCs still outperform SP-compatible TASCs even when ε=0.7.

(2) Performance of real-TARC using the CubeSat model of Figure 3

In the main text, the CubeSat model was used to analyze the performance of TASCs and TARCs. Here, to better assess the performance of realistic TARCs, we performed a case study using published data of TARC from reference 16 (herein termed as "real-TARC"), where α=0.25 is static and ε is temperature-adaptive: ε equal to 0.17 at low T and 0.72 at high T, and the switching temperature is around 23 ℃. Note that the ε of real-TARC is extracted from the Supplementary Information of reference 16. Two non-temperature-adaptive reference materials with the same, static α (0.25) and also static ε (0.17 or 0.72) were also simulated. Similar to Figure 3, the geostationary orbit when the Earth is at the December solstice and the geosynchronous orbit in the ecliptic plane were used for simulation. The corresponding transient temperatures of CubeSats are depicted in Figure S7B and S7E.
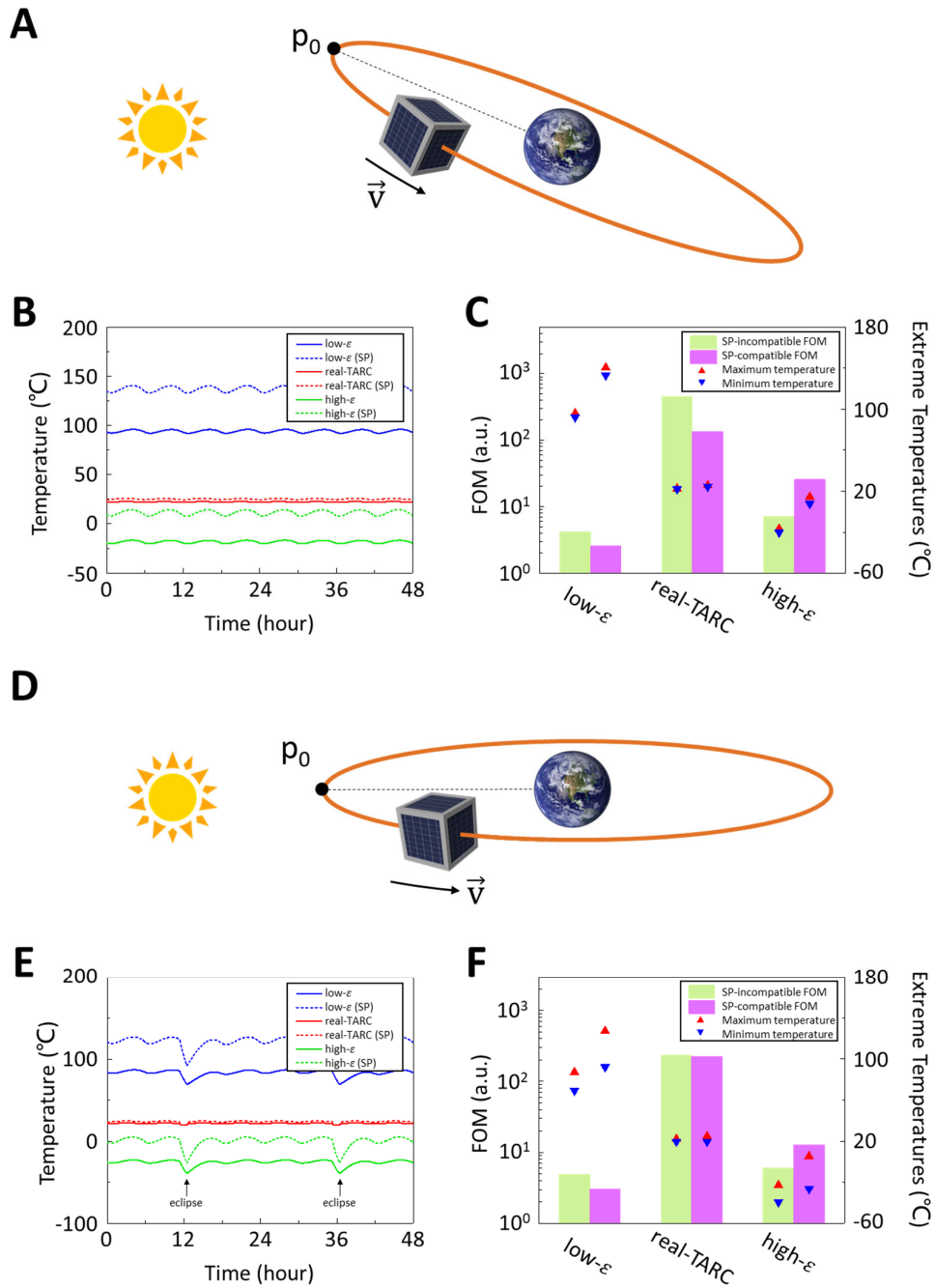
Figure S7. Transient thermal analysis of a 1U-CubeSat covered by real-TARC

(A) A schematic diagram of the geostationary CubeSat model when the Earth is at the December solstice.

(B) Transient temperatures of the geostationary CubeSat covered by real-TARC or references.

(C) Extracted FOMs and extreme temperatures for the cases in (B).

(D) A schematic diagram of the geosynchronous CubeSat model in the ecliptic plane.

(E) Transient temperatures of the geosynchronous CubeSat covered by real-TARC or references.

(F) Extracted FOMs and extreme temperatures for the cases in (E).

Figure S7 shows that real-TARC stabilizes the CubeSat temperature tightly around 23 ℃ and effectively prevents extreme temperature swings caused by direct solar irradiance and solar eclipses. If its solar absorptivity is modified to being SP-compatible, the additional 100% transmission band for SPs imposes only negligible influence on the performance of real-TARC, as supported by the extracted FOM and extreme temperatures (evaluated over one orbital period) in Figure S7C and S7F. For example, the SP-compatibility only worsens the FOM of real-TARC by 3.6% in Figure S7F. Compared with the reference low and high emissivity materials, real-TARC brings in roughly one order of magnitude improvement in both the FOM and the temperature swing.

Note S7. Details for the In-Depth Thermal Analysis of CubeSat

The definition of all six surfaces of CubeSat in Figure 4A (main text) is illustrated in Figure S8. Due to the attitude control of the CubeSat, surface #1 is always directly facing the Earth while surface #5 is always facing the flying direction ($\vec{v}$) of the CubeSat.
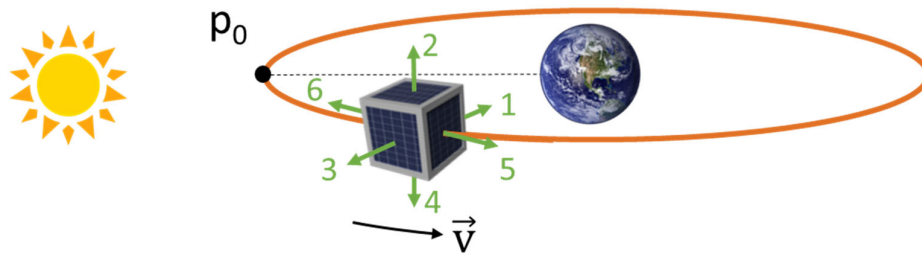

Figure S8. The definition of six surfaces of the CubeSat.

In the main text, we did an in-depth thermal analysis of six solar panels and interior components of a CubeSat covered by TARC. In the simulation, the solar panel on each CubeSat surface has a mass of 0.05 kg and a specific heat capacity of 1000 J/(kg·℃).[27] Since the total mass of the 1U-CubeSat is 1 kg, the mass of interior components of the CubeSat is 0.7 kg. The specific heat capacity of the interior components is set to be 890 J/(kg·℃), because the aluminum structures and the printed circuit boards (PCB) in CubeSats have comparable specific heat capacities.[26,27,35] The thermal resistance between the interior components and the surfaces is 1 K/W in the main text, which can be realized by adjusting the thermal conductance within the CubeSat.

Note S8. Explorative Design for Higher Photovoltaic Efficiencies

The photovoltaic efficiency of SPs increases at lower temperatures.[36] Therefore, it is desirable to design a CubeSat whose interior components (node #7) operate at room temperature while its body-mounted SPs (node #1-#6) stay at much lower temperatures. Here, we present an explorative design for such a CubeSat based on TARCs (Figure S9A). Note that the CubeSat orbit is the same as that used for Figure 4.

First, to stabilize the temperature of SPs at much lower temperatures, we use optimized TARCs with much lower T_{set}=-17 ℃. Secondly, since the operate temperature of node #7 is still

targeted at 23 ℃, node #7 should be more thermally isolated from nodes #1-#6. Finally, to maximize the temperature-regulation performance of SP-compatible TARCs covering the CubeSat, the heat fluxes between the hot SPs and the cold SPs are maximized by increasing the thermal conductance between adjacent SPs.

Based on the above design, the new thermal model for this explorative CubeSat design is presented in Figure S9A. Similar to the model in Figure 4 of the main text, the thermal resistances between node #7 and nodes #1-#6 are denoted as R_1-R_6, respectively. Besides, the thermal conductance between adjacent SPs is improved in this thermal model, and the corresponding thermal resistances (denoted as R_a-R_l) are added to model the inter-SP thermal interaction. Here, the transition temperature range of SP-compatible TARCs is set to be -21 ℃ to -13 ℃, leading to a T_{set}=-17 ℃ for the SPs. The thermal resistances of R_1-R_6 are all 45 K/W while the thermal resistances of R_a-R_l are all 1 K/W. Moreover, the SP-compatible TARCs have temperature-adaptive ε of 0.1-0.9 and static α=0.1.
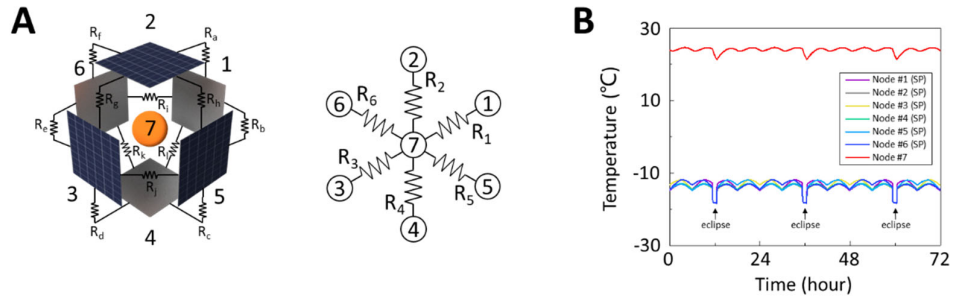

Figure S9. The explorative design of CubeSat for higher photovoltaic efficiencies
(A) A schematic diagram of the new thermal model for the explorative CubeSat design. Similar to the model in Figure 4 of the main text, this model includes the thermal resistances between node #7 and nodes #1-#6 (i.e., R_1-R_6). Apart from them, this model also involves the thermal resistance between adjacent SPs (i.e., R_a-R_l). Note that for clarity, R_1-R_6 are not shown in the left figure and R_a-R_l are not shown in the right figure.
(B) Transient temperatures of nodes #1-#7.

The resultant transient temperatures of nodes #1-#7 are shown in Figure S9B. The interior components still work at optimal temperatures near 23 ℃ with a temperature swing of 3.3 ℃. As a comparison, the temperature swing of node #7 in Figure 4 is 5.3 ℃. The most important advantage of this explorative design lies in the low working temperatures of SPs with small temperature swings: their temperatures merely swing between -18.3 ℃ to -11.8 ℃ even with solar eclipses.
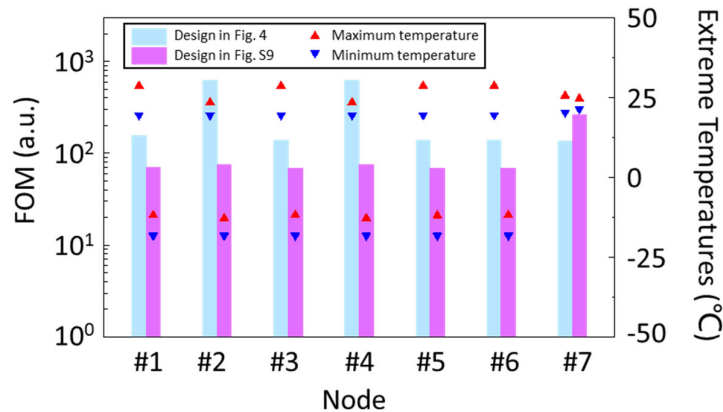
Figure S10. Comparison between the design in Figure 4 and the explorative design in Figure S9

In Figure S10, the FOMs and extreme temperatures of the explorative design are compared with those shown in Figure 4. By optimizing the thermal resistances and SP-compatible TARCs, SPs now work at much lower temperatures for higher PV efficiencies with small temperature swings, while the interior components of the CubeSat is still protected by the stabilized working temperature around 23 ℃.

References

1. Pisacane, V. L. (2003). Spacecraft Systems Design and Engineering. In R. A. Meyers (Ed.), Encyclopedia of Physical Science and Technology (3rd ed.) (pp. 464-483). Elsevier Science Ltd. https://doi.org/10.1016/B0-12-227410-5/00888-7
2. Bulut, M. (2021). Thermal design, analysis, and testing of the first Turkish 3U communication CubeSat in low earth orbit. J. Therm. Anal. Calorim. 143, 4341-4353. https://doi.org/10.1007/s10973-021-10566-z
3. Garzón, A., and Villanueva, Y. A. (2018). Thermal analysis of satellite libertad 2: a guide to cubesat temperature prediction. J. Aerosp. Technol. Manag. 10. E4918. https://doi.org/10.5028/jatm.v10.1011
4. Abdelal, G. F., Abuelfoutouh, N., Hamdy, A., and Atef, A. (2006). Thermal fatigue analysis of small-satellite structure. Int. J. Mech. Mater. 3, 145-159. https://doi.org/10.1007/s10999-007-9019-1
5. Hays, P. B., Abreu, V. J., Dobbs, M. E., Gell, D. A., Grassl, H. J., and Skinner, W. R. (1993). The high-resolution doppler imager on the Upper Atmosphere Research Satellite. J. Geophys. Res. Atmos. 98, 10713-10723. https://doi.org/10.1029/93JD00409
6. Asmar, S. W., Armstrong, J. W., less, L., and Tortora, P. (2005). Spacecraft Doppler tracking: Noise budget and accuracy achievable in precision radio science observations. Radio Sci., 40, 1-9. https://doi.org/10.1029/2004RS003101
7. Thirsk, R., Kuipers, A., Mukai, C., and Williams, D. (2009). The space-flight environment: the International Space Station and beyond. CMAJ, 180, 1216-1220. https://doi.org/10.1503/cmaj.081125

8. Reysa, R., and Thurman, R. (1997, August). The International Space Station ECLS and thermal control systems-Overview. In *Sixth European Symposium on Space Environmental Control Systems*. 40, 11-28. https://adsabs.harvard.edu/pdf/1997ESASP.400...11R

9. Fish, C. S., Swenson, C. M., Crowley, G., Barjatya, A., Neilsen, T., Gunther, J., et al. (2014). Design, development, implementation, and on-orbit performance of the dynamic ionosphere CubeSat experiment mission. Space Sci. Rev, 181, 61-120. https://doi.org/10.1007/s11214-014-0034-x

10. Mason, J. P., Lamprecht, B., Woods, T. N., and Downs, C. (2018). CubeSat on-orbit temperature comparison to thermal-balance-tuned-model predictions. J Thermophys Heat Trans, 32, 237-255. https://doi.org/10.2514/1.T5169

11. Silva, D. F. D., Muraoka, I., and Garcia, E. C. (2014). Thermal control design conception of the Amazonia-1 satellite. J. Aerosp. Technol. Manag., 6, 169-176. https://doi.org/10.5028/jatm.v6i2.320

12. Rao, M. V., Gupta, J. P., Rattan, R., and Thyagarajan, K. (2006, November). RESOURCESAT-2: a mission for Earth resources management. In *GEOSS and Next-Generation Sensors and Missions*, 6407, 119-126. https://doi.org/10.1117/12.697973

13. Dalibot, C., and Tustain, S. (2020, July). The preliminary thermal design for the SPEQTRE CubeSat. In *2020 International Conference on Environmental Systems*. https://ttu-ir.tdl.org/handle/2346/86436

14. Barza, R., Aoki, Y., and Schilling, K. (2006, October). CubeSat UWE-1-technology tests and in orbit results. In *57th International Astronautical Congress*. https://doi.org/10.2514/6.IAC-06-B5.3.07

15. Yang, L., Li, Q., Kong, L., Gu, S., and Zhang, L. (2019). Quasi-all-passive thermal control system design and on-orbit validation of Luojia 1-01 satellite. Sensors, 19, 827. https://doi.org/10.3390/s19040827

16. Tang, K., Dong, K., Li, J., Gordon, M. P., Reichertz, F. G., Kim, H., et al. (2021). Temperature-adaptive radiative coating for all-season household thermal regulation. Science, 374, 1504-1509. https://doi.org/10.1126/science.abf7136

17. Johnston, J. D., and Thornton, E. A. (2000). Thermally induced dynamics of satellite solar panels. J Spacecr Rockets, 37, 604-613. https://doi.org/10.2514/2.3633

18. Shen, Z., and Hu, G. (2013). Thermally induced vibrations of solar panel and their coupling with satellite. Int. J. Appl. Mech., 5, 1350031. https://doi.org/10.1142/S1758825113500312

19. Heidt, H., Puig-Suari, J., Moore, A., Nakasuka, S., and Twiggs, R. (2000). CubeSat: A new generation of picosatellite for education and industry low-cost space experimentation. In *14th Annual/USU Conference on Small Satellites*. https://digitalcommons.usu.edu/cgi/viewcontent.cgi?article=2069&context=smallsat

20. Vitanov, P., Delibasheva, M., Goranova, E., and Peneva, M. (2000). The influence of porous silicon coating on silicon solar cells with different emitter thicknesses. Sol. Energy Mater Sol. Cells. 61, 213-221. https://doi.org/10.1016/S0927-0248(99)00110-5

21. Amores, A. P., Ravishankar, A. P., and Anand, S. (2022, April). Design and Modelling of Metal-Oxide Nanodisk Arrays for Structural Colors and UV-Blocking Functions in Solar Cell Glass Covers. Photonics, 9, 273. https://doi.org/10.3390/photonics9050273

22. Jannat, A., Lee, W., Akhtar, M. S., Li, Z. Y., and Yang, O. B. (2015, June). New and effective anti reflection coating of SiC-SiO2 nanocomposite for p-type silicon solar cell. In *2015 IEEE 42nd*

Photovoltaic Specialist Conference (PVSC) (pp. 1-3).
https://doi.org/10.1109/PVSC.2015.7356325

23. Chen, J. Y., Chang, W. L., Huang, C. K., and Sun, K. W. (2011). Biomimetic nanostructured antireflection coating and its application on crystalline silicon solar cells. Opt. Express, 19, 14411-14419. https://doi.org/10.1364/OE.19.014411

24. Arof, A. K., Noor, I. M., Buraidah, M. H., Bandara, T. M. W. J., Careem, M. A., Albinsson, I., and Mellander, B. E. (2017). Polyacrylonitrile gel polymer electrolyte based dye sensitized solar cells for a prototype solar panel. Electrochim. Acta, 251, 223-234. https://doi.org/10.1016/j.electacta.2017.08.129

25. Kim, H. K., and Han, C. Y. (2010). Analytical and numerical approaches of a solar array thermal analysis in a low-earth orbit satellite. Adv. Space Res., 46, 1427-1439. https://doi.org/10.1016/j.asr.2010.08.023

26. Morsch Filho, E., de Paulo Nicolau, V., de Paiva, K. V., and Possamai, T. S. (2020). A comprehensive attitude formulation with spin for numerical model of irradiance for CubeSats and Picosats. Appl. Therm. Eng., 168, 114859. https://doi.org/10.1016/j.applthermaleng.2019.114859

27. Vega Martinez, S., Filho, E. M., Seman, L. O., Bezerra, E. A., Nicolau, V. D. P., Ovejero, R. G., and Leithardt, V. R. Q. (2021). An integrated thermal-electrical model for simulations of battery behavior in CubeSats. Appl. Sci., 11, 1554. https://doi.org/10.3390/app11041554

28. AAUSAT-4. (2022, July 11). spaceflight101. https://spaceflight101.com/spacecraft/aausat-4/

29. AAUSAT 3, 4, 5. (2022, July 11). Gunter's Space Page. https://space.skyrocket.de/doc_sdat/aausat-3.htm

30. Kopacz, J. R., Herschitz, R., and Roney, J. (2020). Small satellites an overview and assessment. Acta Astronaut., 170, 93-105. https://doi.org/10.1016/j.actaastro.2020.01.034

31. Fröhlich, C., and Brusa, R. W. (1981). Solar radiation and its variation in time. Sol. Phys., 74, 209-215. https://doi.org/10.1007/BF00151291

32. Kovács, R., and Józsa, V. (2018). Thermal analysis of the SMOG-1 PocketQube satellite. Appl. Therm. Eng., 139, 506-513. https://doi.org/10.1016/j.applthermaleng.2018.05.020

33. Hernández-Gómez, J. J., Yanez-Casas, G. A., Torres-Lara, A. M., Couder-Castañeda, C., Orozco-del-Castillo, M. G., Valdiviezo-Navarro, J. C., et al. (2019, November). Conceptual low-cost on-board high performance computing in CubeSat nanosatellites for pattern recognition in Earth's remote sensing. In Proceedings of the 1st International Conference on Geospatial Information Sciences, 13, 114-122. https://doi.org/10.29007/8d25

34. CanX-7 (Canadian Advanced Nanospace eXperiment-7). (2022, July 11). ESA Earth Observation Portal. https://directory.eoportal.org/web/eoportal/satellite-missions/c-missions/canx-7

35. Malde, C. K., Sharma, G., and Aneesh, A. M. (2021, March). Development and Testing of Computational Model for the Thermal Analysis of a CubeSat Nanosatellite. In *2021 IEEE Aerospace Conference (50100)* (pp. 1-9). https://doi.org/10.1109/AERO50100.2021.9438451

36. Fesharaki, V. J., Dehghani, M., Fesharaki, J. J., and Tavasoli, H. (2011, November). The effect of temperature on photovoltaic cell efficiency. In *Proceedings of the 1st International Conference on Emerging Trends in Energy Conservation–ETEC*, Tehran, Iran (pp. 20-21). https://research.iaun.ac.ir/pd/jjfesharakiold/pdfs/PaperC_4124.pdf